Icarus 236 (2014) 92–103

Contents lists available at ScienceDirect

Icarus

journal homepage: www.elsevier.com/locate/icarus

Latitudinal structure of the Venus O_2 infrared airglow: A signature of small-scale dynamical processes in the upper atmosphere

J.-C. Gérard [a,*], L. Soret [a], G. Piccioni [b], P. Drossart [c]

[a] LPAP, Université de Liège, Liège, Belgium
[b] IAPS, INAF, Rome, Italy
[c] Observatoire de Paris-Meudon, Paris, France

ARTICLE INFO

Article history:
Received 20 December 2013
Revised 17 March 2014
Accepted 17 March 2014
Available online 3 April 2014

Keywords:
Venus, atmosphere
Atmospheres, dynamics
Atmospheres, structure
Infrared observations

ABSTRACT

Images of the nightside limb of Venus have been obtained in the northern hemisphere with the VIRTIS multispectral infrared imager on board Venus Express between April 2006 and October 2008. We analyze the latitudinal distribution of the $O_2(a^1\Delta)$ airglow limb profiles at 1.27 μm to characterize its distribution and variability. We show that the instantaneous structure of the emission is very different from the statistical global view of an enhanced emission near the equator, decreasing in brightness and slightly increasing in altitude toward the poles. The peak intensity of the limb profiles varies by a factor up to 50 between the brightest spots and the darkest regions. The bright airglow spots correspond to regions of enhanced downward flow of oxygen atoms originating from the dayside. Considerable variations in brightness and morphology are observed in the altitude–latitudinal distribution over a 24-h period. Analysis of the limb profiles indicates that secondary airglow peaks located at altitudes higher than the mean value of 96 km are observed on about 30% of the latitudinal cuts, but they are concentrated in narrow latitude areas extending over a few hundred kilometers. Most of them occur in transition regions between two altitude regimes in the 50° to 60°N region, possibly associated with the drop of the cloud top altitude observed equatorward of the "cold collar". We interpret these results as an indication that the strength of vertical transport in this mesosphere–thermosphere transition region is very variable both in location and time. This variability, also observed in nadir airglow images and wind measurements, is a key characteristic of the mesosphere–thermosphere transition region. It may be caused by fluctuations of the global day-to-night circulation generated by gravity waves. We show with a one-dimensional model that local enhancements of eddy transport is a possibility. This variability is currently not accounted for by global circulation models that predict a single stable region of enhanced airglow in the vicinity of the antisolar point.

1. Introduction

Connes et al. (1979) first observed the presence of the O_2 infrared airglow at 1.27 μm on both day and night sides of Venus with nearly equal intensity. They proposed that the observed emission corresponds to radiative relaxation of the $O_2(a^1\Delta)$ metastable molecules to the ground-state following three-body recombination of oxygen atoms. They suggested that the atoms are produced on the Venus dayside by photodissociation and electron impact dissociation of CO_2 and CO and transported to the nightside by the subsolar to antisolar circulation (SSAS). This global SSAS circulation transports the O and N atoms from the lower thermosphere near the subsolar point to higher altitudes where the recombination rates between atoms are much lower. The downward flow near the antisolar point then carries atomic oxygen back to the upper mesosphere where the O and CO_2 densities increase, the atoms recombine and emit photons. The reaction scheme may be written:

$$2O + CO_2 \xrightarrow{k} O_2^* + CO_2 \quad (1)$$

$$O_2^* \xrightarrow{A_{1\Delta}} O_2 + h\nu \quad (2)$$

$$O_2^* + CO_2 \xrightarrow{C_q} O_2 + CO_2 \quad (3)$$

where O_2^* represents excited oxygen molecules; k is the reaction rate coefficient of reaction (1) taken to be 3.1×10^{-32} cm^6 s^{-1} and

* Corresponding author. Address: Laboratoire de Physique Atmosphérique et Planétaire (LPAP), Université de Liège, 17, allée du 6 août, Bat. B5c, 4000 Liège, Belgium. Fax: +32 42669711.
E-mail address: jc.gerard@ulg.ac.be (J.-C. Gérard).

http://dx.doi.org/10.1016/j.icarus.2014.03.028
0019-1035/

obtained by multiplying the experimental value with N_2 as a background gas at 187 K (Huestis et al., 2008) by a factor 2.5 (Nair et al., 1994). This temperature is the mean result of several studies implying different methods summarized in Table 3 of Bailey et al. (2008) and Krasnopolsky (2010); $A_{1_\Delta} = 2.19 \times 10^{-4}\ s^{-1}$ is the Einstein coefficient of the 1.27 μm transition; C_q is the quenching coefficient, for which only an upper limit of $2 \times 10^{-20}\ cm^{-3}\ s^{-1}$ has been set (Sander et al., 2003).

Other weaker O_2 airglow emissions resulting from processes (1)–(3) have also been observed on the Venus nightside (Migliorini et al., 2013 and ref. therein).

The global circulation of the Venus upper atmosphere is generally described as a combination of two components: a superrotating zonal flow below the cloud top (about 70 km) altitude and the previously described subsolar-to-antisolar flow in the lower thermosphere above 120 km (Dickinson and Ridley, 1977; Bougher and Borucki, 1994; Lellouch et al., 2008; Clancy et al., 2012a). The transition region between the two regimes is still poorly known, although substantial progress has been made during the last few years both theoretically and observationally. In situ or remote measurements of the distribution of constituents have indicated the accumulation of atoms or molecules in regions of the nightside thermosphere (Niemann et al., 1980; Schubert et al., 2007; Clancy et al., 2012b). Series of airglow measurements made with instruments on board Venus Express have confirmed and complemented earlier measurements made during the Pioneer Venus era (Stewart et al., 1980). Observations of the ultraviolet nitric oxide nightglow indicated an accumulation of nitrogen atoms carried on the nightside by the SSAS global circulation, but shifted 2–3 h dawnward by the presence of a statistical retrograde zonal wind. Whether this thermospheric zonal wind is an upward extension of the zonal circulation observed near the cloud top or a different regime disconnected from that prevailing at lower altitude is still an open question. Alexander (1992) suggested that gravity waves generated in the clouds region are able to force the zonal flow much above the cloud top and account for the presence of zonal winds in the thermosphere.

Three-dimensional thermospheric general circulation models coupling transport and chemistry models have been developed to validate and understand the concept of global circulation in the Venus upper atmosphere. Early three-dimensional model studies suggested that the circulation above about 90 km is dominated by a subsolar to antisolar flow, with upwelling over the subsolar point, rapid flow across the terminator and subsidence near the antisolar point (Dickinson and Ridley, 1977; Bougher et al., 1988). Considerable success was obtained with more recent versions of the Venus Thermospheric General Circulation Model (VTGCM) (Bougher et al., 1990; Brecht et al., 2011, 2012) which included a zonal wind component. They were able to reproduce the observed day–night thermal contrast, the average intensity of the NO and O_2 nightglow emissions and their horizontal and vertical distribution. However, the flow across the terminators is decelerated using a Rayleigh friction scheme which has no clear physical interpretation.

When all nadir observations at 1.27 μm made with the Visible and InfRared Thermal Imaging Spectrometer (VIRTIS) instrument on board Venus Express are co-added to provide a global view of the airglow distribution on the Venus nightside, a statistical picture emerges. The airglow is statistically characterized by a region of enhanced intensity centered on the antisolar point. This bright statistical region is about four times brighter than the average nadir intensity of about 0.5 MR (Piccioni et al., 2009; Soret et al., 2012). By contrast, Hueso et al. (2008) and Piccioni et al. (2009) showed that, in individual nadir observations, the O_2 airglow structure is complex and shows significant deviations from its globally averaged distribution on the nightside. Soret et al. (in press) analyzed in detail individual VIRTIS nadir images and showed that bright zones are observed at nearly any nightside location and move at speeds up to 100 ms^{-1}, while changing brightness and shape. However, individual spots are generally more intense in the vicinity of the anti-solar point than closer to the terminator. These spotty regions of enhanced O_2 intensity are believed to correspond to zones of maximum supply of atomic oxygen into the recombination region (Allen et al., 1992; Crisp et al., 1996; Ohtsuki et al., 2008; Soret et al., in press). Inhomogeneous structures in the distribution of the OH Meinel $\Delta v = 1$ airglow around 3 μm highly correlate in brightness (Soret et al., 2010) and morphology (Gérard et al., 2012) with those of the O_2 IR airglow. A large daily variability was also observed in the morphology of the nitric oxide airglow observed with the ultraviolet spectrometer on board Pioneer Venus (Stewart et al., 1980) and the SPICAV instrument on board Venus Express (Gérard et al., 2008; Stiepen et al., 2013). The peak of the NO limb profiles is statistically located near 115 km, that is 15–20 km higher than the O_2 infrared airglow. Comparisons between model and data suggested a highly variable Venus wind system in the lower thermosphere, with intermittently strong variations in nightside eddy diffusion. These two emissions may be viewed as tracers of the global circulation in the Venus upper mesosphere and lower thermosphere in two different regimes. The NO ultraviolet nightglow is mostly controlled by the SSAS transport of O and N atoms from the dayside along streamlines above 140 km on the dayside, and down to 115 km on the nightside (Bougher and Borucki, 1994). Similarly, the O_2 emissions are produced by recombination of O atoms created above 110 km on the dayside, which travel across the terminator and recombine near 96 km on the nightside (Drossart et al., 2007a; Gérard et al., 2009a, 2010; Piccioni et al., 2009). At a given time, the two emissions generally show no spatial correlation as was shown by comparing simultaneous SPICAV and VIRTIS nadir observations (Gérard et al., 2009b).

The observed airglow inhomogeneity suggests that the thermospheric global circulation may be considerably more complex than a simple SSAS Hadley-type cell. Alexander (1992) suggested that the observed variability may be associated with gravity wave-induced turbulence which modifies the local supply of O atoms over periods of a few hours. Bougher and Borucki (1994) argued that the upward propagating gravity waves can modulate the dayside supply of mesospheric O atoms and the intensity of the flow across the terminator. This mechanism could produce temporal variations in the eddy diffusion coefficient in the lower thermosphere by modifying the altitude at which the waves break.

Following a description of the VIRTIS-M observations used in this study (Section 2), we provide additional evidence and constraints for the importance of the inhomogeneity and variability of the transport of constituents from the day to the night side and/or local nightside inhomogeneous vertical transport. We also show that the vertical distribution of the O_2 airglow may change dramatically over relatively limited latitudinal distances. The sensitivity of emission limb profiles to local turbulent transport, parameterized by eddy diffusion in one-dimensional models, is discussed in Section 3. We also show how transitions between altitude regimes may coincide with limb profiles with double peaks and their relationship to the presence of upward propagating gravity waves.

2. VIRTIS observations

The limb images analyzed in this study were obtained with the VIRTIS-M spectral imager on board the Venus Express satellite. The Venus Express spacecraft has been orbiting Venus since April 2006 on an elliptical orbit with a period of 24 h, an apocenter at

66,000 km and a pericenter near 250 km, located at 80°N (Svedhem et al., 2007). The orbit is fixed in inertial space so that it precesses in local time and covers a full cycle in a Venus year. Spectral images of the planetary limb have been obtained with the VIRTIS instruments.

The VIRTIS instruments have been described by Drossart et al. (2007b) and Piccioni et al. (2009) and the Venus Express modes of observation by Titov et al. (2006). VIRTIS is composed of two spectrometers: the VIRTIS-M imaging spectrometer at medium spectral resolution and the VIRTIS-H high spectral resolution spectrometer. VIRTIS-H did not cover the 1.27 μm spectral region and will not be discussed any further here. VIRTIS-M infrared provides spectral cubes between 0.25 and 5 μm at a spectral resolution ~9.8 nm at 1.27 μm. A spatial scan, covering a ~64 mrad field of view, is generally obtained in about 30 min using a scanning mirror. The integration time for each spectrum and limb vertical sampling ranges between 0.36 s and 8 s. The 0.25 mrad pixel size of the VIRTIS-M detector projected on Venus limb provides a spatial resolution of 15 km from apocenter and 1.9 km for a spacecraft distance of 7500 km, a value typical of a VIRTIS observation at 40° in the northern hemisphere. In this study, we only use images where the field of view intercepts the limb from a distance of less than 15,000 km. Thermal radiation from the lower atmosphere produces a background contribution when observing at the nadir but analysis of the spectral cubes in the vicinity of 1.27 μm at the limb indicates that this contribution is very small for altitudes of the tangent point above ~85 km and thermal background corrections are negligible above 90 km (Piccioni et al., 2009).

The individual VIRTIS observation sequences last generally on the order of 30 min, so that these images may be approximately considered as snapshots of the $O_2(a^1\Delta)$ infrared airglow distribution in a range of latitudes at a given local time. Individual limb profiles of the $O_2(a^1\Delta)$ emission are then extracted from the limb images by range of 1° of the α parameter defined as the angular abscissa associated to each pixel, following the method described by Gérard et al. (2010). Each image is then divided into bands of increasing angular abscissa of width $\Delta\alpha = 1°$. Each band provides a series of pixels that may be sorted according to the value of their tangent altitude. These data points are then grouped into 1 km altitude bins to generate the limb profile associated with an average latitude and local time. The subtraction of the instrumental background signal is made through the VIRTIS data processing pipeline and the small residual background contribution occasionally present in the extracted limb profiles above the altitude of the airglow emissions is removed. Each limb profile is visually inspected to remove those presenting spurious instrumental noise. The limb brightness of the emission at 1.27 μm is expressed in MegaRayleighs (1 MR = 1×10^{12} photon/cm^2 s emitted in 4π steradians). These profiles are then deconvolved to account for the finite spatial field of view of the instrument that smears out the actual limb profile. As these limb profiles vary in latitude, vertical profiles are finally extracted after the data points have been merged into bins 1° of latitude wide. When the latitudinal coverage provided by the set of sequences obtained during an orbit is sufficient (at least 10° of latitude), series of adjacent VIRTIS-M images of the night limb are assembled to provide latitudinal syntheses of the O_2 airglow limb profile (Fig. 1a). Some latitudes have not been observed for operational reasons (such as to prevent excessive heating of the VIRTIS detector), causing data gaps in the composite latitudinal view, as seen near 14° in Fig. 1a. In other cases, latitude sectors are viewed twice and the data in the region of overlap are then averaged. We note that, as a consequence of the eccentricity of the orbit with its pericenter near the north pole, only data collected in the northern hemisphere are used to construct this database. A total of 132 orbits (between orbit 25 and orbit 907) include at least partial nightside limb view. All limb images have been processed,

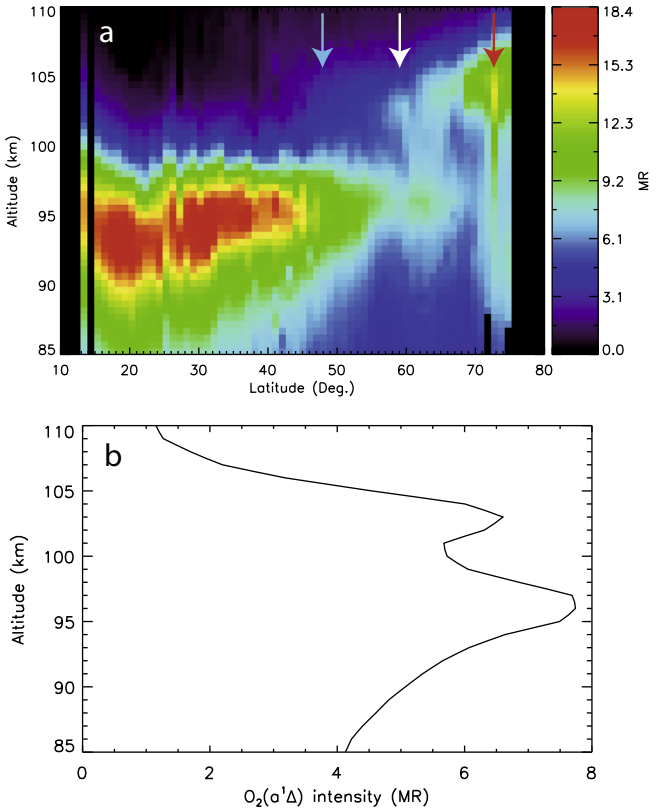

Fig. 1. (a) Latitudinal–vertical distribution of the $O_2(a^1\Delta)$ limb intensity at 1.27 μm observed along orbit 320. The observations have been grouped into bins of 1 km altitude × 1° of latitude. Note the striking change of the layer altitude between 60° and 65°N, where the emission peak jumps from 95 km to about 104 km over a narrow range of latitudes. The region used to extract the limb profile in Fig. 1b is indicated by the white arrow. The blue and red arrows indicate the latitudes of the two profiles shown in Fig. 7. (For interpretation of the references to color in this figure legend, the reader is referred to the web version of this article.)

covering a period extending from May 2006 to October 2008. A total of 66 orbits, including a total of 161 limb imaging sequences, contain useful information that is covering at least 10° of latitude. The F10.7 cm daily solar activity index for Earth, a proxy for the EUV solar flux intensity, averaged over the days when observations were collected was ~72×10^{-22} W m^{-2} Hz^{-1}. Examples of limb intensity distributions were previously shown by Piccioni et al. (2009) and Gérard et al. (2009b).

3. Latitudinal airglow structures

Statistics on the latitudinal distribution of the peak intensity of the limb profiles used in this study is shown in Fig. 2. The data have been binned into 1° of latitude cells. The 1-σ variability within each bin is indicated by the vertical bar. Neglecting the southern latitude and high northern latitudes bins which contain only a small sample, the emission peak altitude appears to abruptly increase between 42° and 46°. The average value is 95.6 km between 0° and 42° (1591 limb profiles) and 97.1 km between 46° and 74° (752 profiles). The test of significance for these two means indicates that they are significantly different at a confidence level exceeding 99.99%.

This trend is in agreement with the results shown in Fig. 6 of Soret et al. (2012) indicating that the peak of the O density also tends to move upward toward the poles. A powerful way to view the latitudinal variations of the O_2 airglow is to analyze images of the nightside limb directly obtained by VIRTIS as will be done hereafter.

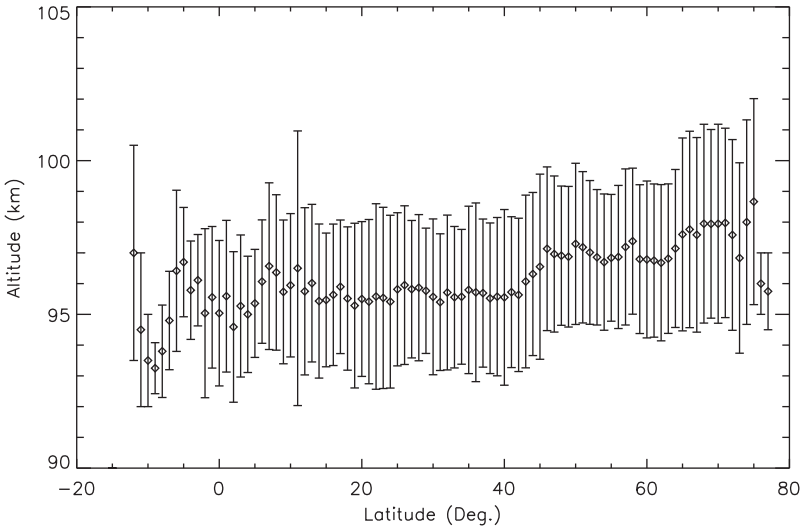

Fig. 2. Latitudinal distribution of the altitude of the mean $O_2(^1\Delta)$ emission peak observed at the limb by VIRTIS-M between May 2006 and October 2008. The data have been binned into 1° wide cells. The vertical bars indicate the size of the 1-σ variability. Note the change of altitude between 42° and 46°.

As mentioned before, different observing modes and targets of the VIRTIS instruments were used during the lifetime of the instrument. Consequently the number of periods when latitudinal observations closely spaced in time have been made is limited. Three time series combining 7, 7 and 2 latitudinal cuts respectively are presented in Figs. 3–5. Note that no limb data were collected for some dates. The dates, times, latitude and local time ranges of the Venus Express orbits illustrated in these figures are listed in Table 1.

Fig. 3 shows the 7 latitudinal distributions collected over an 11-day period, including 5 consecutive orbits (panels b, c, d, e and f). Each color scale is indicated by the vertical coded bars to the right of the panels and may be different for each panel, but easily comparable. In each case, the latitudinal distribution is far from homogeneous with strong variations of the peak location and intensity. In panel (a), the center of the bright spot is close to 95 km up to about 60° but moves up by a few kilometers at higher latitudes. Three days later (panel b and Fig. 1a) the peak intensity has dropped by a factor of 4.5 and the spot has extended towards higher latitudes. Three VIRTIS sequences (or sessions) were used to build this composite image. This latitudinal cut shows three different regions. The first one, which extends from 13° to 52° in the midnight sector, is typical of the O_2 airglow behavior observed during the Venus Express mission: the peak lies in the vicinity of 95 km, with a moderate increase of its altitude and a drop of the intensity with increasing latitude. A second region (58–68°) is a transition and shows a double peak over a limited latitude sector (10° wide). The vertical distribution suddenly changes near 60° and the peak emission jumps by about 10 km. Finally, in the higher latitude zone, the peak remains near 104 km and the limb brightness increases, reaching a maximum of 13.6 MR at 73°N with a long downward streak of airglow extending down to below 90 km. The local time covered by this set of observations varied from 01:00 at 13° to 03:00 at 75°. Note that, at these high latitudes, the distance between the midnight and the 3 a.m. meridians is quite limited. It is important to note that the transition region is observed within a single VIRTIS sequence (VI0320_05, from 50° to 75°) and is thus not an artifact of a time discontinuity in the data collection. A zoomed version of panel b was presented in Fig. 1a. The white arrow indicates the transition region presenting a second peak located at higher altitude than the main maximum at 96 km. The limb profile extracted at 62°N is plotted in Fig. 1b. The secondary peak is nearly as bright as the main peak, but slightly narrower. We note that this profile was interpreted by Piccioni et al. (2009) as a signature of upward propagating gravity waves.

On the next day (panel c), the high latitude peak has brightened and its structure has changed into a broader region with two distinct maxima. A similar pattern is observed 24 h later (panel d) where three bright regions, separated by about 25° of latitude, have appeared. The spot at 19° is still located a few kilometers lower than the two at higher latitudes. The next orbit (panel e) exhibits an enhanced emission at 100 km, whereas the last images of the set of consecutive orbits (panel f) shows the sudden appearance of five spots, all with slightly different peak altitudes, separated by distances of 10–15°, or 1000–1500 km as they are located along the same meridian. Finally, 3 days later (panel g), a single bright spot remains near 20°, while the higher latitude emission quickly drops in altitude and intensity beyond 30°.

Fig. 4 presents a similar set of latitudinal cuts covering over a period of 22 days. The brightness color scale is identical for all 6 latitudinal cuts. This set of observations confirms the variability of the vertical–latitudinal intensity over periods of days. A striking example of localized enhancements is seen in the 50° sector between panels (e and f) where the intensity increases from about 15 to 45 MR in 48 h. The presence of sharp latitudinal gradients in the brightness of the $O_2(a^1\Delta)$ emission is also confirmed , for example in panels (c and f).

Fig. 5 clearly illustrates the appearance of an additional bright spot near 30° over a 48-h time span. In panel (a), a bright region is observed centered near 14° at 98 km. It shows a fairly sharp poleward boundary near 35°, with an intensity dropping below 15 MR at 40°. Two days later, the pattern has considerably changed. The center of the initial bright spot has moved equatorward and a second enhanced region localized around 30° has developed. The spot near the equator now shows a steep increase of the peak altitude (5 km over 15° of latitude) in the poleward direction, whereas the additional enhanced region around 30° show an equally fast altitude drop with increasing latitude. The lack of time continuity between the two datasets and the absence of data beyond 70° in orbit 497 make it impossible to determine whether the poleward spot between 50° and 60° in orbit 499 corresponds to (i) a motion toward the equator of a potential enhanced region present in orbit 497 beyond 70°, (ii) a motion toward the pole of part of the enhanced region of orbit 497, or (iii) the development of a newly formed bright region.

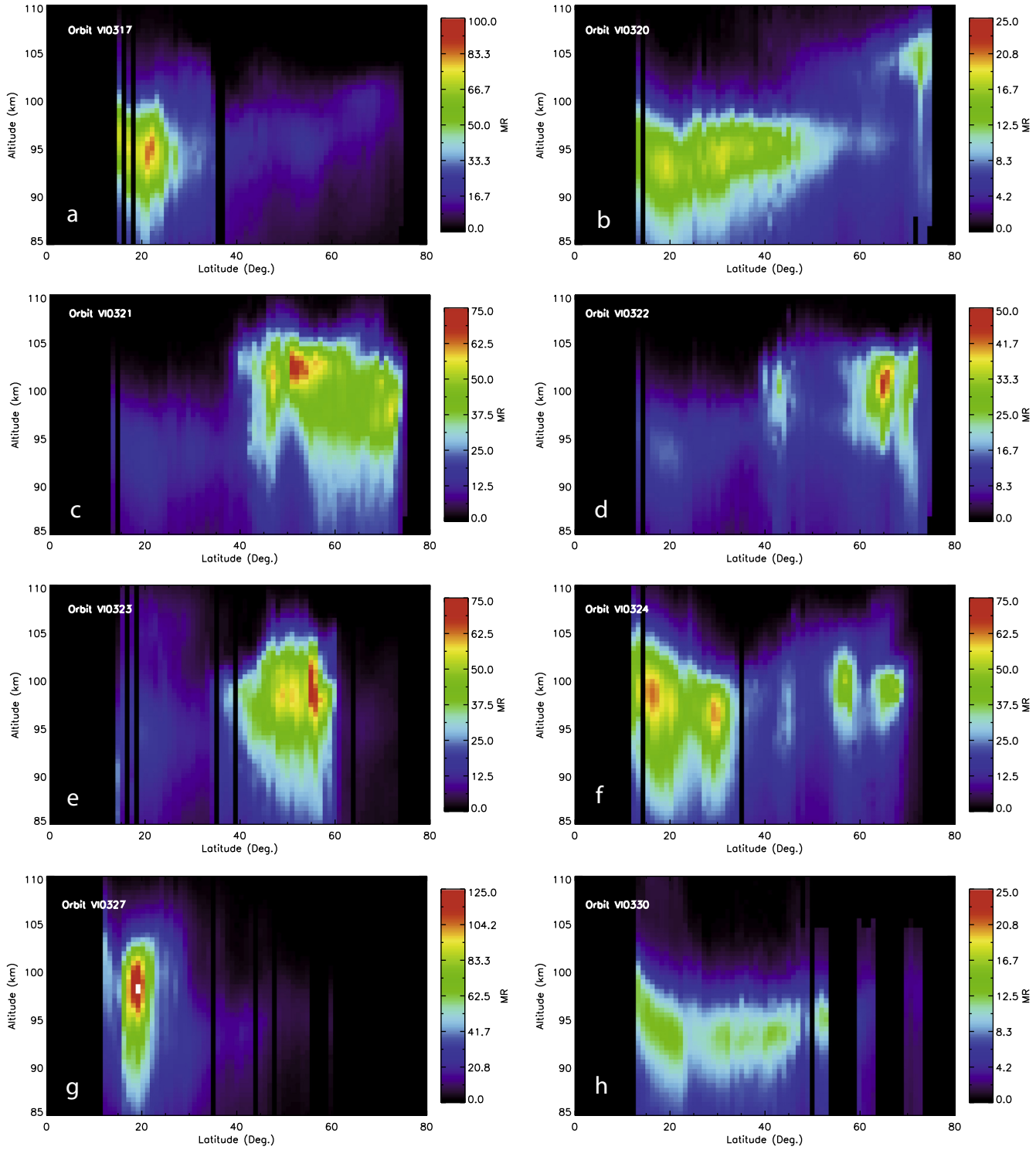

Fig. 3. Time sequence of limb images showing the latitude–altitude distribution of the $O_2(^1\Delta)$ emission. Each orbit is separated by 24 h. This sequence illustrates the morphological variations observed over a total time span of 10 days. The color scale is different for each panel, but easily comparable. Some features persist from one day to the next, although detailed morphology and the relative brightness may change. Dramatic variations are also observed such as between orbits 323 and 324. Note the complexity of the latitudinal distribution exhibiting multiple spots, such as observed during orbit 324.

In summary, the vertical distribution of the O_2 infrared airglow along meridional cuts shows a great deal of inhomogeneity. Abrupt changes in the altitude of the emission peak indicate that the density distribution of atomic oxygen and possibly CO_2 may occur over distances of a few hundred kilometers. In particular, Fig. 3 panels a, b, d, f, g and h, and Fig. 4 panels a, e and f show a trend with increasing altitude of the maximum intensity as northern latitude increases. The study by Gérard et al. (2010) and Fig. 2 of this paper also suggest that the same conclusion is statistically observed, although Fig. 3c is a counter-example with an altitude drop of 6 km between 50° and 75°N. Soret et al. (2012) also noted a tendency of the altitude of the O density peak to increase with latitude. Multiple peaks are occasionally observed along the meridian cuts, in agreement with previous studies of the $O_2(a^1\Delta)$

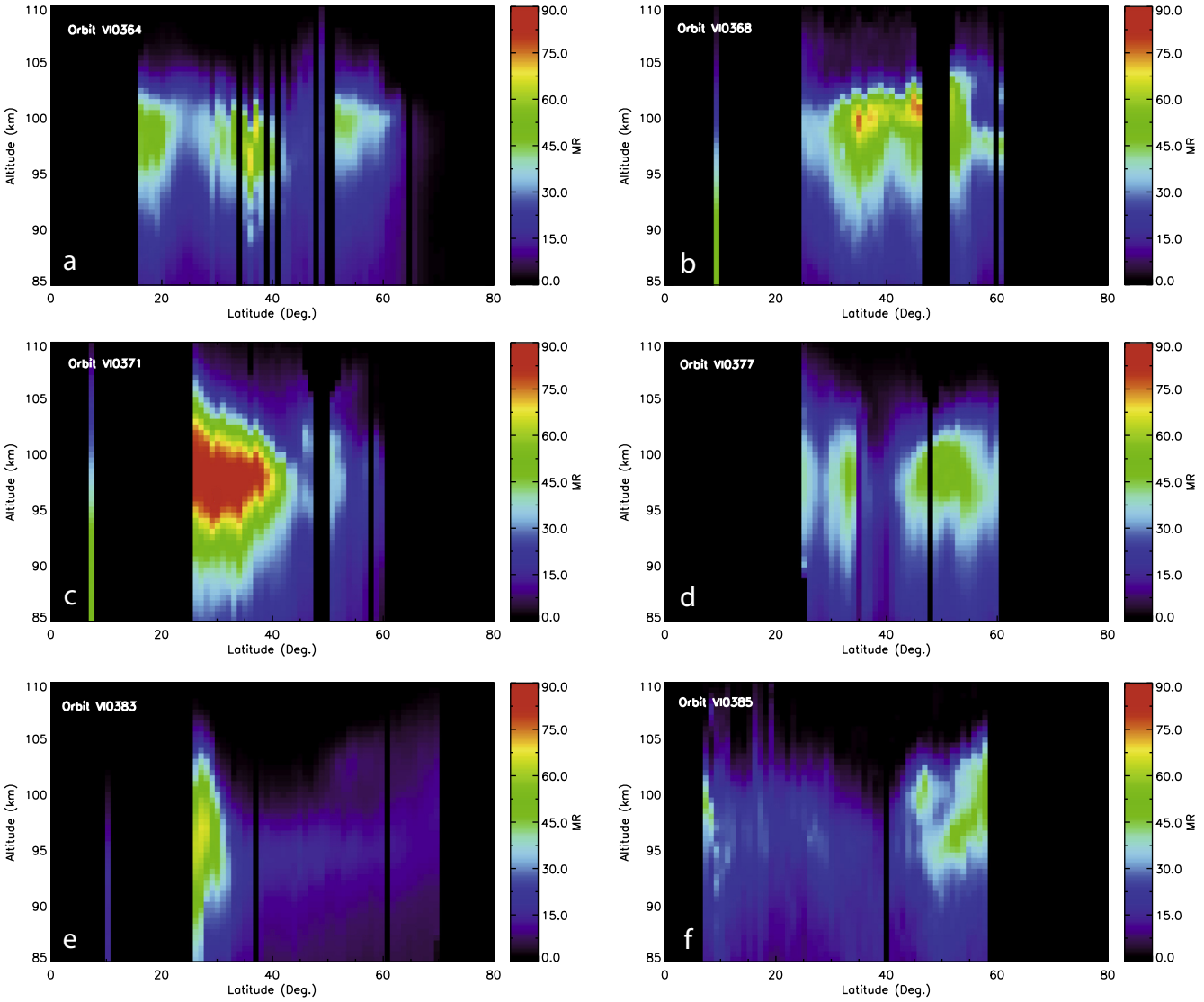

Fig. 4. Time sequence of limb images showing the latitude–altitude distribution of the $O_2(^1\Delta)$ emission. A total of 11 days separate the first and the last plots. The color scale is identical for all panels.

airglow morphology based on nadir ground-based (Bailey et al., 2008) and VIRTIS observations (Soret et al., in press). A quasi-periodicity in the horizontal distance between successive peaks is sometimes observed, as in Fig. 3d, f, h and Fig. 4a. We finally note that, although they are presented in a two-dimensional latitude–altitude space, these latitudinal cuts are the result of the integration of the volume emission rate along the line of sight. Therefore the bright spots are not necessarily located along the same meridian. However, the weight of the atmospheric regions in the integral decreases with the distance from of the tangent point.

4. Sources of airglow inhomogeneity and variability

Observations described before show clear evidence that the instantaneous distribution of the $O_2(a^1\Delta)$ Venus nightglow may be very different from the statistical global picture obtained when summing individual nadir images (Piccioni et al., 2009; Soret et al., 2012). Multiple bright spots frequently occur simultaneously at several locations with different spatial extension, brightness and altitude distribution. These features suggest that transport from the day to the night side is more complex and time dependent than currently implemented in steady state three-dimensional models such as the VTGCM (Bougher et al., 1990; Brecht et al., 2011). Multiple spots observed with VIRTIS in the nadir mode may change morphology and direction independently from each other, even though they are located in similar sectors of the planet's nightside (Hueso et al., 2008; Soret et al., in press).

Secondary peaks in limb profiles are occasionally observed in narrow latitudinal regions, such as in Figs. 1a and 4f. A total of 22 occurrences have been identified during the period of VIRTIS-M IR observations. This number must be compared with the 132 Venus Express orbits including IR limb images, 66 of which include data with continuous coverage over at least 10° of latitude. It is important to note that the latitudinal extent of regions with secondary emission peaks is considerably less than 22/66, since those zones presenting a secondary peak generally correspond to at most a few percent of the latitudinal coverage of each image. Remarkably, these regions are rarely observed at low or mid-latitudes. They are generally located in the vicinity of 50°N, mostly between 50° and 60°. As was shown by Taylor et al. (1980), this location corresponds to the region of the cold collar observed in the latitude range 50–75° at the cloud top where temperatures drop from 250 to as low as 210 K (Piccioni et al., 2007). It is also close to

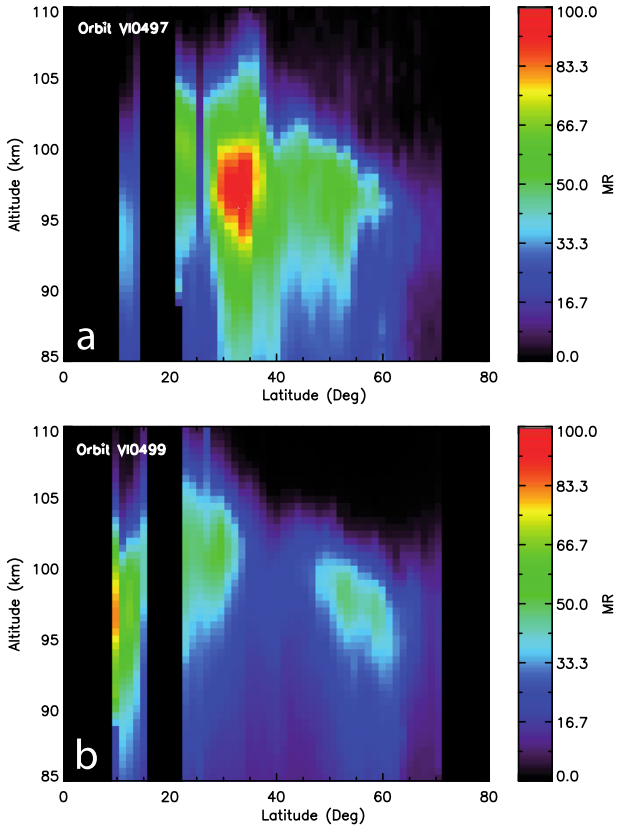

Fig. 5. Set of limb images showing the latitude–altitude distribution of the $O_2(^1\Delta)$ emission. Two days separate the first and the second plot. Note the gap between 35° and 45° observed on orbit 499 but not present two orbits earlier. The color scale is identical for both panels.

the equatorward boundary of the region where the altitude of the cloud top starts dropping with increasing latitude (Ignatiev et al., 2009). In any case, it is likely that the change of altitude observed in Fig. 2 in this region is the statistical signature of this change of altitude regime. Double peaks have been interpreted as possible signatures of gravity waves vertically redistributing the oxygen concentration (Piccioni et al., 2009). Our results now indicate that they frequently occur in regions close to a distinct discontinuity in the airglow limb profile. This point will be further discussed in Section 4.2.

In this section, we first examine the quantities that control the vertical distribution of the $O_2(a^1\Delta)$ density, and the altitude of the peak intensity of the 1.27 μm emission. We then discuss the occurrence of multiple peaks in the limb profiles and their possible relationship with the presence of gravity waves in the mesosphere–thermosphere transition region.

4.1. One-dimensional modeling of the $O_2(^1\Delta)$ airglow vertical distribution

In order to quantify the effect of different factors on the changes of altitude of the emission peak described before, we use the one-dimensional model described by Gérard et al. (2008). Although a quantitative description of the global transport and circulation in the Venus upper atmosphere requires three-dimensional modeling, 1-D models are useful to assess the importance of selected physical quantities on the vertical distribution of atomic oxygen and the O_2 airglow profile. In brief, the model solves the set of continuity equations to obtain the steady state vertical distribution of the density of $O(^3P)$, $N(^4S)$ atoms, NO and $O_2(a^1\Delta)$ metastable molecules:

$$\frac{\partial n_i}{\partial t} = -\frac{\partial \Phi_i}{\partial z} + P_i - L_i - \frac{\partial (n_i w)}{\partial z} \tag{4}$$

where z is the altitude, t is time, n_i is the number density of constituent I, Φ_i its vertical downward flux, P_i is the production rate of species i, L_i the loss rate and w is the vertical wind velocity, positive upward.

The vertical diffusive flux is given by:

$$\phi_i = -(D_i + K)\left(\frac{\partial n_i}{\partial z} + \frac{n_i}{T}\frac{\partial T}{\partial z}\right) - \left(\frac{D_i}{H_i} + \frac{K}{H}\right) n_i \tag{5}$$

with T the neutral gas temperature, D_i the molecular diffusion coefficient for constituent i, K the vertical eddy diffusion coefficient, H_i the local scale height of the i constituent, H the atmospheric scale height. The last term in Eq. (5) corresponds to the vertical advection flux. Eq. (4) with the flux expression ϕ_i from (5) is solved numerically between 130 and 80 km using the finite volume method on a constant altitude grid. A flux boundary condition through the upper boundary is applied for O and N, and we assume photochemical equilibrium at the lower boundary for all four species. We use density null vectors for initial conditions (except at the boundaries). The choice of the densities at 80 km is relatively arbitrary and we verified that it does not influence the solution further than one scale height from the lower boundary for a reasonable range of values. At the upper boundary, we leave the $O(^3P)$ and the $N(^4S)$ downward fluxes as free parameters to be determined by fitting the modeled limb profile to the observations, although we impose a flux ratio $\Phi_O/\Phi_N = 100$. The model is then parameterized by the values of A, $w(z)$ and Φ_O. The chemical reactions controlling the P_i and L_i terms, and the rate coefficients used in the model are those listed by Soret et al. (2012) and Gérard et al. (2008). An additional process, namely the N + O → NO ($C\,^2\Pi$) reaction, plays a key role in the production of the UV nitric oxide airglow in the gamma and delta bands. However, this reaction is considerably slower than reaction (1) and only makes a negligible contribution as a chemical sink of O atoms.

The eddy diffusion coefficient K is assumed to depend on the inverse square root of the total neutral density in the form $K = A/n^{1/2}$, where K is expressed in $cm^2\ s^{-1}$ and n, the total number density, in cm^{-3}. A value of $K \sim 1.4 \times 10^{13}/n^{1/2}$ (in cgs units, with n in cm^{-3}) was derived from the analysis of the neutral composition measured with the Bus Neutral Mass Spectrometer (BNMS) instrument on board the Pioneer Venus bus which penetrated the dayside atmosphere at low latitude (60° solar zenith angle) (von Zahn et al., 1980). A value of $A = 8 \times 10^{12}$, with an uncertainty of 50% was derived from measurements of the NO nightglow limb profile with the Pioneer Venus Ultraviolet Spectrometer by Gérard et al. (1981). Values ranging from 0 to 7.4×10^{11} were determined by Gérard et al. (2008), based on a study of limb profiles of the nitric oxide nightglow obtained with the SPICAV instrument on board Venus Express. The best fit to the globally averaged NO airglow limb profile observed with SPICAV corresponds to $A = 1 \times 10^{11}$ (Stiepen et al., 2013). Slightly different values of the rate coefficients and of the A constant were used in photochemical models (Krasnopolsky, 2013) but the following conclusions are independent of the minor differences.

Series of model runs were made (Table 2) to investigate the influence of the boundary conditions and the value of the A constant on the altitude of the emission peak. In summary, these simulations indicate that in the one-dimensional modeling approach:

1. The downward flux of N atoms Φ_N has little influence on the peak density and altitude of the vertical distribution of the O_2 airglow layer. Increasing Φ_N from 1×10^8 to $1 \times 10^{10}\ cm^{-2}\ s^{-1}$ while keeping Φ_O constant changes the emission peak altitude

Table 1
Location and time of the VIRTIS-M limb images used to provide the latitudinal cuts shown in Figs. 1 and 3–5.

Orbit number	Sequence	UT (yyyy.mm.dd)	Latitude (°)	Local time (h)	Number of vertical profiles
VI0317	06	2007.03.04	14.75–33.5	0.7–0.3	20
	07	2007.03.04	25.3–49.7	0.4–0.3	21
	08	2007.03.04	47.6–74.9	0.2–2.7	32
VI0320	03	2007.03.07	12.8–33.4	1.0–0.6	22
	04	2007.03.07	25.2–49.6	0.7–0.6	25
	05	2007.03.07	47.5–74.9	0.0–3.0	32
VI0321	03	2007.03.08	12.7–33.3	1.1–0.7	22
	04	2007.03.08	25.2–49.6	0.8–0.7	25
	05	2007.03.08	47.5–74.9	0.7–3.1	32
VI0322	01	2007.03.08	14.9–15	20.0–20.0	2
	06	2007.03.09	12.7–33.3	1.2–0.8	22
	07	2007.03.09	25–49.4	0.9–0.8	25
	08	2007.03.09	47.4–74.7	0.8–3.2	32
VI0323	01	2007.03.09	13.7–14	19.6–19.7	3
	06	2007.03.10	14.6–33.4	1.3–0.9	20
	07	2007.03.10	25.2–49.6	1.0–0.9	25
	08	2007.03.10	47.4–73.5	0.9–2.9	30
VI0324	06	2007.03.11	12.5–33	1.5–1.0	22
	07	2007.03.11	25.1–49.6	1.2–1.0	25
	08	2007.03.11	47.4–72.7	1.0–2.9	29
VI0327	05	2007.03.14	11.9–33.3	1.8–1.4	23
	06	2007.03.14	25.1–48.5	1.5–1.4	24
	07	2007.03.14	47.3–59.9	1.3–1.7	10
VI0330	04	2007.03.17	12.6–33	2.1–1.7	22
	05	2007.03.17	24.9–49.3	1.8–1.7	25
	06	2007.03.17	48.4–73	1.7–3.6	13
VI0364	07	2007.04.20	15.9–32.3	21.4–21.7	18
	08	2007.04.20	29.5–48.6	21.7–21.7	20
	09	2007.04.20	52.4–71.3	21.6–19.9	23
VI0368	01	2007.04.23	8.9	23.7	1
	08	2007.04.24	25.2–60.7	22.2–21.8	32
VI0371	01	2007.04.26	6.9–6.7	23.7–23.6	2
	10	2007.04.27	25.8–60.3	22.6–22.1	33
VI0383	01	2007.05.08	9.9	3.5	1
	12	2007.05.09	26.2–70.3	23.8–22.5	47
VI0385	06	2007.05.11	9.7–16.3	23.5–0.0	11
	07	2007.05.11	7.3–58.2	23.5–0.1	51
VI0497	09	2007.08.31	42.7–6.3	0.8–23.8	40
	10	2007.08.31	19.6 to −2	0.3–23.2	8
VI0499	11	2007.09.02	43.5–6.9	1.1–0.1	40
	12	2007.09.02	19.8 to −3.4	0.5–23.3	12

Table 2
Dependence of the peak brightness and altitude of the airglow emission at 1.27 μm to the values of vertical wind velocity w (in cm s^{-1}), the vertical flux of O and N atoms (in cm^{-2} s^{-1} at 130 km) and the A constant of the eddy diffusion coefficient.

w (80,100,130 km)[a]	Φ_N	Φ_O	A	Peak intensity (MR)	Peak altitude (km)
(0,0,0)	2.2×10^9	2.2×10^{11}	4.0×10^{13}	8.0	93.5
(0,−3.5,−3.5)	2.2×10^9	2.2×10^{11}	4.0×10^{13}	7.7	93.0
(0,−7,−7)	2.2×10^9	2.2×10^{11}	4.0×10^{13}	5.6	90.5
(0,0,0)	2.2×10^9	2.2×10^{11}	4.0×10^{14}	2.6	87.0
(0,0,0)	2.2×10^9	2.2×10^{11}	2.0×10^{13}	9.6	95.5
(0,0,0)	2.2×10^9	2.2×10^{11}	4.0×10^{12}	11.7	100.5
(0,0,0)	2.2×10^9	2.2×10^{11}	$0–1.0 \times 10^{10}$	13.5	108.0
(0,0,0)	1.0×10^9	1.0×10^{11}	4.0×10^{12}	5.2	99.0
(0,0,0)	1.0×10^{10}	1.0×10^{12}	4.0×10^{12}	55.6	102.5
(0,0,0)	1.0×10^8	1.0×10^{12}	4.0×10^{12}	55.6	102.5
(0,0,0)	2.6×10^9	2.6×10^{11}	2.0×10^{13}	11.5	95.5
(0,0,0)	2.4×10^9	2.4×10^{11}	1.2×10^{12}	13.6	104.0

[a] Values of the vertical wind velocity at 80, 100 and 130 km. The wind profile is linearly interpolated between these values.

by less than 0.5 km. This is because the three-body recombination process (1) is the main loss process for O atoms in the region of interest here, far more important than the reaction with N(^{4}S) atoms.

2. The vertical advection velocity w influences the altitude of the O_2 layer, moving down the $O_2(a^1\Delta)$ emission layer as the downward wind velocity increases. For example, the emission peak drops from 95.5 km to 93 km and 90.5 km if the (constant)

vertical wind velocity w increases from 1.75 to 3.5 and 7 cm s^{-1} respectively for $\Phi_O = 2.2 \times 10^{11}$ cm^{-2} s^{-1} and $A = 4 \times 10^{13}$. However, in the absence of any measurement of the vertical wind in this region, we limit our simulations to the $w = 0$ case.

3. The peak $O_2(a^1\Delta)$ density (and the corresponding limb intensity) increases in a quasi-linear manner with the value of Φ_O, for a given value of the A parameter. For example, for a fixed value $A = 4 \times 10^{12}$, the altitude of the $O_2(a^1\Delta)$ maximum limb intensity ranges from 5.2 MR for $\Phi_O = 1 \times 10^{11}$ cm^{-2} s^{-1} to 55 MR for $\Phi_O = 1 \times 10^{12}$ cm^{-2} s^{-1}. This quasi-linear dependence versus the O atom flux stems from the fact that nearly every two O atoms flowing down will give rise to an O_2 molecules, 75% of which produce a 1.27 μm photon, as long as quenching of the $a^1\Delta$ state by CO_2 remains negligible.
4. The main control of the altitude of the emission peak is through the value of the A coefficient in the eddy transport parameterization. It varies from 108 km for $A = 0$, to 100.5 km for $A = 4 \times 10^{12}$ and 94 km for $A = 2 \times 10^{12}$, for a constant O flux through the upper boundary of 1×10^{11} cm^{-2} s^{-1}. Fig. 6 illustrates the calculated limb profiles of the 1.27 μm emission for this set of A values. As can be readily seen, when the strength of eddy mixing increases, the peak altitude drops and the peak intensity concurrently decreases. Actually, the column emission rate also drops as quenching of the $O_2(a^1\Delta)$ state by collisions with CO_2 increases with increasing pressure.

We now apply the model to the specific case of the VIRTIS observations made during orbit 320 (Fig. 1a). Specifically, emission limb profiles are extracted on either side of the transition region at 48°N and 73°N (blue and red arrows in Fig. 1a) and plotted as solid lines in Fig. 7. Although the peak intensities are quite similar, they show distinct altitude characteristics. The profile at 48° peaks at 96 km (profile #1), a value close to the global mean altitude of 96.4 km. The profile extracted at 73° shows a high altitude peak, close to 104 km (profile #2). The dotted lines show the model curves best fitting these two observations for $w = 0$. They were obtained with the following set of parameters:

- Profile 1: $\Phi_O = 2.6 \times 10^{11}$ cm^{-2} s^{-1}, $A = 2 \times 10^{13}$.
- Profile 2: $\Phi_O = 2.4 \times 10^{11}$ cm^{-2} s^{-1}, $A = 1.2 \times 10^{12}$.

We note that the simulations with the one-dimensional model (Fig. 6) indicate that the altitude of the airglow layer is close to 110 km for the case $A = 0$ corresponding to no vertical transport (photochemical equilibrium). The altitude of the observed

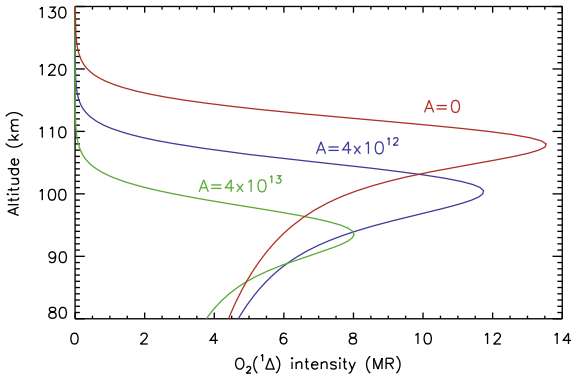

Fig. 6. One-dimensional simulation of the $O_2(^1\Delta)$ emission limb profile based on the one-dimensional model (see text) and sensitivity to the strength of the eddy-diffusion coefficient K (A coefficient in the expression of K). The value of the downward flux of O atoms through the 130 km level is set equal to 1×10^{11} atoms cm^{-2} s^{-1}.

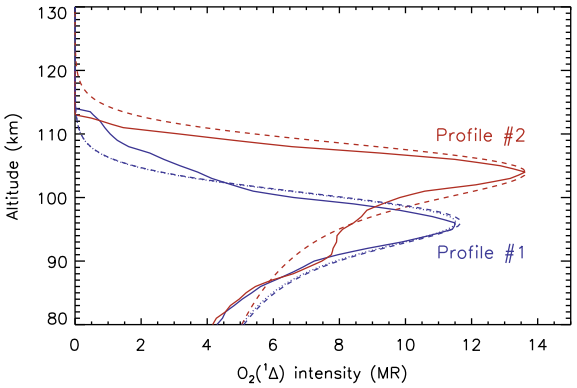

Fig. 7. One-dimensional simulation of the $O_2(^1\Delta)$ emission limb profile observed during orbit 320 at two different latitudes. The solid lines correspond to the observed limb profiles and the dotted lines are the modeled profiles best fitting the observations. The corresponding O atom fluxes and eddy diffusion parameter values are discussed in the text.

maximum intensity in the limb profiles is always below 105 km (Gérard et al., 2010; Soret et al., 2012). This comparison suggests that no region with upward motion was observed in the VIRTIS data set. Consequently, areas of low airglow intensity probably correspond a reduced or a null downward transport, but no signature of O atom uplifting has been observed with VIRTIS.

4.2. Role of global and local dynamics

Nadir observations of the $O_2(a^1\Delta)$ nightside airglow directly relate to the features described in Section 3. For example, the ground-based measurements by Allen et al. (1992), Crisp et al. (1996) and Bailey et al. (2008) already suggested that the actual instantaneous airglow structure may be considerably different from its long-term statistical picture, with bright features observed over a wide range of latitudes and local times. The size of the localized regions of intense airglow typically varies from 500 to 2000 km (Crisp et al., 1996; Soret et al., in press). Dramatic spatial and temporal variations were observed with characteristic lifetimes of about less than day. Evidence for such rapid changes in the airglow distribution is dramatically illustrated with the sequence of orbits 321–324 in Fig. 3. Crisp et al. (1996) indicate that very dark airglow regions are often adjacent to brightest features. The intensities in the high intensity regions often vanish almost entirely within one day. As noted on the basis of the present results, similar situations are also seen in almost all of the VIRTIS latitudinal cuts in Figs. 3–5. These airglow enhancements are univocally tied to enhanced concentrations of atomic oxygen in the region of the airglow production. A direct temperature effect on the efficiency of the O + O + M process is very unlikely as temperature measurements directly derived from the rotation distribution of the $a^1\Delta \rightarrow X\ ^3\Sigma$ (0–0) band show only limited variations as was summarized by Bailey et al. (2008). Variations of a few Kelvins are too small to significantly affect the recombination coefficient of reaction (1). Two scenarios may be considered as likely sources of O_2 airglow (and O density) inhomogeneity on the nightside:

(a) time variations in the global transport from the day to the night side generated by the global SSAS circulation,
(b) spatially variable efficiency of the turbulent downward transport on the nightside in the mesosphere–thermosphere transition region.

In the first case, the local supply of O atoms significantly varies over few hours as a consequence of time dependent global flow

pattern. Steady state three-dimensional modeling is by essence unable to numerically assess the importance of such processes. However, a recent study by Zalucha et al. (2013) analyzed the role of gravity waves generated in the cloud region. They concluded that these vertically propagating waves are unable to reach the upper mesosphere and are either reflected or absorbed.

In the second scenario, the variations occur much closer to the airglow region. They are associated with fast changes in the turbulent transport or the advection velocity field that carries O atoms from the thermosphere into the atomic oxygen loss region. As seen in Figs. 3–5, the emission peaks are located below 105 km.

Simulations such as reported in Fig. 6 clearly indicate that molecular diffusion alone is not able to move the airglow layer down to the region near 95–100 km where the airglow is generally observed (Fig. 2). Therefore, we suggest that the zones associated with intensity enhancements correspond to regions of downwelling and dark areas to region with upward or reduced downward flow. These local effects probably superimpose and perturb the global SSAS circulation and produce the series of bright and darker regions previously described. At this point, further three-dimensional modeling with self-induced variability would be required to address this question.

5. Double peaks in limb profiles

We now concentrate on the possible occurrence of secondary peaks sometimes observed in the $O_2(a^1\Delta)$ altitude profiles and examine their possible origin. We first recall that in this analysis, about 1/3 of the latitudinal cuts exhibit the presence of a narrow latitudinal region with a secondary peak. We note here some differences with other airglow analyses, which partly explain the small number of such occurrences. First, we extract one limb profile every 1° of latitude from a VIRTIS observation. In this way, we avoid constructing latitudinally averaged limb profiles mixing regions corresponding to different regimes of O_2 airglow distribution. Second, we restrict our analysis to directly observed limb profiles without performing Abel inversion producing volume emission rate profiles. The inversion procedure may generate additional secondary peaks, corresponding to inflections in the observed limb profiles.

Several mechanisms may generate multiple peaks in airglow limb profiles.

1. lack of spherical symmetry in the airglow layer vertical distribution,
2. inhomogeneous vertical transport strength by eddy mixing,
3. time dependent downward flow of O atoms at different locations,
4. upward propagating gravity waves.

The first explanation directly stems from the observed uneven distribution of the 1.27 μm emission across the planetary nightside. If two regions with enhanced intensity are observed at the limb along the same line of sight, they will produce an apparent double peak structure in the observed limb profile. If the altitude of the two layers is identical, the bright region located further along the line of sight will generate a secondary peak apparently located below the "true" altitude of the emitting layer. The geometry of such observations was illustrated and discussed in the study of the Venus nitric oxide airglow by Royer et al. (2010). If the two layers are located at different altitudes, integration along the line of sight will produce a double peak in the limb profile. Piccioni et al. (2009) discussed the effects of this second possibility on the relative brightness of the two emission peaks and disregarded this explanation on the basis of the morphology of the airglow structures.

The second scenario requires the use of a one-dimensional model or two- (or three-) dimensional models. We present hereafter model simulations to assess the possibility that some of the features of the vertical latitudinal features described in Section 3, including the presence of double peaks, are generated by spatially variable vertical transport. We examined the third possibility using two-dimensional simulations based on the model described by Collet et al. (2010). In this scenario, the line of sight crosses two regions of enhanced O vertical flux with a different time history: one has reached the region near 95 km while the second one is still descending toward the three-body recombination region. However, the simulations show that a significant emission rate is only produced within less than 1 km of the altitude of the first peak altitude. Therefore, time-dependent oxygen supply in itself is unable to generate a secondary peak if vertical transport is homogeneous.

Evidence of the presence of gravity waves signatures in the Venus upper atmosphere was obtained in Pioneer Venus probe and Orbiter Atmospheric Drag data. During re-entry of the PV spacecraft in the nightside lower thermosphere, Kasprzak et al. (1993) found horizontal wave structures with a wavelength ranging from 100 to 600 km in the ONMS data, with amplitudes depending on the molecular weight of the species, including O and CO_2. The VIRTIS instrument on Venus Express has observed perturbations in the CO_2 dayglow emissions. Garcia et al. (2009) showed that CO_2 non-LTE emissions with a wavelength of 4.3 μm originating from the 110–140 km altitude level show wave-like perturbations of about 0.5% amplitude of the background signal with horizontal wavelengths in the 90–400 km range. They found that the wave geographical distribution and the orientation of wave fronts indicate that the polar vortex in the cloud layer is the source of these gravity waves and demonstrate the strong influence of the polar vortex on the circulation in the atmosphere of Venus up to the thermosphere. The amplitudes of these observed vertical and horizontal density perturbations is clearly too small to generate the airglow structures reported here. Zhang et al. (1996) showed that the simulated distribution of the O_2 airglow is strongly sensitive to small changes of the characteristic intrinsic phase speeds at the lower boundary. They claimed that this sensitivity implies that minor variations in gravity wave momentum fluxes to the thermosphere can produce large temporal and spatial variations of the $O_2(a^1\Delta)$ emission, in agreement with observations.

Hoshino et al. (2012) developed a general circulation model (GCM) for the mesosphere and thermosphere. Their GCM simulations indicated that among the planetary-scale waves (thermal tides, Rossby and Kelvin waves), the Kelvin waves are the only ones causing a temporal variation in the wind velocity at the altitude of the O_2 1.27 μm nightglow. Their simulations suggest that Kelvin waves could cause temporal variations in the nightglow emission antisolar region with an intensity of 1.1–1.3 MR and a period of approximately 4 days. Zalucha et al. (2013) implemented the gravity wave-drag parameterization of Alexander and Dunkerton (1999) into the VTGCM to investigate breaking gravity waves as a source of momentum deposition in Venus' thermosphere. They could not find a combination of wave parameters bringing the calculated density and nightglow emissions into agreement with the observations. They found that gravity waves generated below 100 km do not propagate into the jet core regions where atmospheric drag is needed. They concluded that parameterizations developed for the middle atmosphere do not work in the thermosphere. They suggested that appropriate damping mechanisms other than nonlinear breaking or saturation dominate and should be accounted for at thermospheric altitudes. Horizontal wave propagation could also play an important role. The possible role played by gravity waves in the generation of multiple O_2 airglow peaks was recently discussed by Altieri et al. (submitted for publication).

6. Conclusions

The latitudinal–vertical airglow distributions presented in this study, combined with previous ground-based and space-borne observations of the nitric oxide and O_2 nightglow make it possible to point out some of the characteristics of the transport properties of the Venus nightside transition region:

1. The subsolar to antisolar general circulation controls the statistical behavior of the O_2 infrared nightglow on time scales of months and years. It carries a substantial fraction of the O atoms created on the dayside to the nightside, with a maximum supply in the vicinity of the antisolar point.
2. Snapshot pictures of the oxygen nightglow distribution are very different from long-term averaged observations. Regions of enhanced emission are observed at nearly all latitudes and local times. They are likely associated with small-scale regions of increased downward flow of O atoms.
3. The strongest enhancements are generally located at low latitudes near the midnight sector, reaching as much as 6 times the average nightside brightness. However bright spots are also seen at mid- and high latitudes.
4. Dramatic changes in the morphology and intensity of the O_2 airglow are observed over a 24-h period, but features may also persist longer.
5. Significant changes of altitude regime are observed within a few degrees of latitude. The altitude of the bright regions is not clearly different from that observed in zones of weaker O_2 emission. Airglow profiles showing a secondary peak are generally observed inside these transition regions between 50° and 60°N. These are possibly related to the presence of the cold collar surrounding both polar regions.
6. Simulations indicate that the altitude of the airglow layer is very sensitive to the strength of the downward transport (advection or turbulent). The altitude of the emission peak does not exceed 105 km, a value below that calculated for photochemical equilibrium with null vertical transport. This upper limit suggests that regions of upward transport did not occur during the periods of VIRTIS limb imaging.

The changing limb morphology and intensity observed over a 24-h period, combined with the spatial structure differences along the meridian, indicates that, in addition to the large-scale SSAS circulation, small-scale motions play a major role in the distribution of constituents. This control is present on a large fraction of the Venus nightside. It creates inhomogeneity in NO and O_2 airglow emissions, temperature, and CO mixing ratio (Stewart et al., 1980; Soret et al., 2012; Ohtsuki et al., 2008; Clancy et al., 2012b). The sources of these local enhancements (gravity waves, downwelling, enhanced eddy mixing) are still largely unknown. Monitoring of the Venus nightside NO and O_2 emissions with dedicated airglow imagers in future space missions appears as a crucial next step to clarify the sources and characteristics of the spatial and temporal variability. It will be possible to simultaneously follow short timescale variations and wind regimes at two different altitudes.

References

Alexander, M.J., 1992. A mechanism for the Venus thermospheric superrotation. Geophys. Res. Lett. 22, 2207–2210.

Alexander, M.J., Dunkerton, T.J., 1999. A spectral parameterization of mean-flow forcing due to breaking gravity waves. J. Atmos. Sci. 56, 4167–4182.

Allen, D., Crisp, D., Meadows, V.S., 1992. Variable oxygen airglow on Venus as a probe of atmospheric dynamics. Nature 359, 516–519.

Altieri, F., Migliorini, A., Zasova, L., Shakun, A., Piccioni, G., Bellucci, G., 2014. Modeling of VIRTIS/VEX $O_2(a^1\Delta_g)$ nightglow profiles affected by the propagation of gravity waves in the Venus upper mesosphere. J. Geophys. Res. (submitted for publication).

Bailey, J., Chamberlain, S., Crisp, D., Meadows, V.S., 2008. Near infrared imaging spectroscopy of Venus with the Anglo-Australian Telescope. Icarus 56, 1385–1390.

Bougher, S.W., Borucki, W.J., 1994. Venus O_2 visible and IR nightglow: Implications for lower thermosphere dynamics and chemistry. J. Geophys. Res. 99, 3759–3776.

Bougher, S.W., Roble, R.G.E., Dickinson, R.E., Ridley, E.C., 1988. Venus mesosphere and thermosphere. III—Three-dimensional general circulation with coupled dynamics and composition. Icarus 73, 545–573.

Bougher, S.W., Gérard, J.C.A.I.F., Stewart, A.I.F., Fesen, C.G., 1990. The Venus nitric oxide night airglow: Model calculations based on the Venus thermospheric general circulation model. J. Geophys. Res. 95, 6271–6284. http://dx.doi.org/10.1029/JA095iA05p06271.

Brecht, A.S., Bougher, S.W., Gérard, J.-C., Parkinson, C.D., Rafkin, S., Foster, B., 2011. Understanding the variability of nightside temperatures, NO UV and O_2 IR nightglow emissions in the Venus upper atmosphere. J. Geophys. Res. 116, 8004. http://dx.doi.org/10.1029/2010JE003770.

Brecht, A., Bougher, S.W., Gérard, J.-C., Soret, L., 2012. Atomic oxygen distributions in the Venus thermosphere: Comparisons between Venus Express observations and global model simulations. Icarus 217, 759–766.

Clancy, R.T., Sandor, B.J., Moriarty-Schieven, G., 2012a. Circulation of the Venus upper mesosphere/lower thermosphere: Doppler wind measurements from 2001–2009 inferior conjunction, sub-millimeter CO absorption line observations. Icarus 217, 794–812.

Clancy, R.T., Sandor, B.J., Moriarty-Schieven, G., 2012b. Thermal structure and CO distribution for the Venus mesosphere/lower thermosphere: 2001–2009 inferior conjunction sub-millimeter CO absorption line observations. Icarus 217, 779–793.

Collet, A., Cox, C., Gérard, J.C., 2010. Two-dimensional time-dependent model of the transport of minor species in the Venus night side upper atmosphere. Planet. Space Sci. 58, 1857–1867.

Connes, P., Noxon, J.F., Traub, W.A., Carleton, N.P., 1979. $O_2(^1\Delta)$ emission in the day and night airglow of Venus. Astrophys. J. 233, 29–32.

Crisp, D., Meadows, V.S., Bézard, B., deBergh, C., Maillard, J.P., Mills, F.P., 1996. Ground-based near-infrared observations of the Venus nightside: 1.27 μm $O_2(a^1\Delta_g)$ airglow from the upper atmosphere. J. Geophys. Res. 101, 4577–4593.

Dickinson, R.E., Ridley, E.C., 1977. Venus mesosphere and thermosphere temperature structure: II. Day-night variations. Icarus 30, 163–178.

Drossart, P. et al., 2007a. Scientific goals for the observation of Venus by VIRTIS on ESA/Venus Express mission. Planet. Space Sci. 55, 1653–1672.

Drossart, P. et al., 2007b. Infrared spectral imaging observations of Venus by VIRTIS reveal a dynamical upper atmosphere. Nature 450, 641–645.

Garcia, R.F., Drossart, P., Piccioni, G., López-Valverde, M., Occhipinti, G., 2009. Gravity waves in the upper atmosphere of Venus revealed by CO_2 nonlocal thermodynamic equilibrium emissions. J. Geophys. Res. 114, E00B32. http://dx.doi.org/10.1029/2008JE003073.

Gérard, J.-C., Stewart, A.I.F., Bougher, S.W., 1981. The altitude distribution of the Venus ultraviolet airglow and implications on vertical transport. Geophys. Res. Lett. 8, 633–636.

Gérard, J.-C., Cox, C., Saglam, A., Bertaux, J.-L., Villard, E., Nehmé, C., 2008. Limb observations of the ultraviolet nitric oxide nightglow with SPICAV on board Venus Express. J. Geophys. Res. 113, E00B03. http://dx.doi.org/10.1029/2008JE003078.

Gérard, J.-C., Saglam, A., Piccioni, G., Drossart, P., Montmessin, F., Bertaux, J.-L., 2009a. Atomic oxygen distribution in the Venus mesosphere from observations of O_2 infrared airglow by VIRTIS–Venus Express. Icarus 199, 264–272.

Gérard, J.-C. et al., 2009b. Concurrent observations of the ultraviolet nitric oxide and infrared O_2 nightglow emissions with Venus Express. J. Geophys. Res. 114, E00B44.

Gérard, J.-C., Soret, L., Saglam, A., Piccioni, G., Drossart, P., 2010. The distributions of the OH Meinel and $O_2(a^1\Delta–X^3\Sigma)$ nightglow emissions in the Venus mesosphere based on VIRTIS observations. Adv. Space Res. 45, 1268–1275.

Gérard, J.-C., Soret, L., Piccioni, G., Drossart, P., 2012. Spatial correlation of OH Meinel and O_2 infrared atmospheric nightglow emissions observed with VIRTIS-M on board Venus Express. Icarus 217, 813–817.

Hoshino, N., Fujiwara, H., Takagi, M., Takahashi, Y., Kasaba, Y., 2012. Characteristics of planetary-scale waves simulated by a new Venusian mesosphere and thermosphere general circulation model. Icarus 217, 818–830.

Hueso, R. et al., 2008. Morphology and dynamics of Venus oxygen airglow from Venus Express/Visible and Infrared Thermal Imaging Spectrometer observations. J. Geophys. Res. 113, E00B02.

Huestis, D.L. et al., 2008. Cross sections and reaction rates for comparative planetary aeronomy. Space Sci. Rev. 139, 63–105.

Ignatiev, N.I. et al., 2009. Altimetry of the Venus cloud tops from the Venus Express observations. J. Geophys. Res. 114, E00B43. http://dx.doi.org/10.1029/2008JE003320.

Kasprzak, W.T., Niemann, H.B., Hedin, A.E., Bougher, S.W., Hunten, D.M., 1993. Neutral composition measurements by the Pioneer Venus Neutral Mass Spectrometer during Orbiter re-entry. Geophys. Res. Lett. 20, 2747–2750. http://dx.doi.org/10.1029/93GL02241.

Krasnopolsky, V.A., 2010. Venus night airglow: Ground-based detection of OH, observations of O_2 emissions, and photochemical model. Icarus 207, 17–27.

Krasnopolsky, V.A., 2013. Nighttime photochemical model and night airglow on Venus. Planet. Space Sci. 85, 78–88.

Lellouch, E., Paubert, G., Moreno, R., Moullet, A., 2008. Monitoring Venus' mesospheric winds in support of Venus Express: IRAM 30-m and APEX observations. Planet. Space Sci. 56, 1355–1367.

Migliorini, A., Piccioni, G., Gérard, J.-C., Soret, L., Slanger, T.G., Politi, R., Snels, M., Drossart, P., Nuccilli, F., 2013. The characteristics of the O_2 Herzberg II and Chamberlain bands observed with VIRTIS/Venus Express. Icarus 223, 609–614.

Nair, H., Allen, M., Anbar, A.D., Yung, Y.L., 1994. A photochemical model of the martian atmosphere. Icarus 111, 124–150.

Niemann, H.B., Kasprzak, W.T., Hedin, A.E., Hunten, D.M., Spencer, N.W., 1980. Mass spectrometric measurements of the neutral gas composition of the thermosphere and exosphere of Venus. J. Geophys. Res. 85, 7817–7827. http://dx.doi.org/10.1029/JA085iA13p07817.

Ohtsuki, S. et al., 2008. Distributions of the Venus 1.27 μm O_2 airglow and rotational temperature. Planet. Space Sci. 56, 1391–1398.

Piccioni et al., 2007. South-polar features on Venus similar to those near the north pole. Nature 450, 637–640.

Piccioni, G. et al., 2009. Near-IR oxygen nightglow observed by VIRTIS in the Venus upper atmosphere. J. Geophys. Res. 114. http://dx.doi.org/10.1029/2008je003133.

Royer, E., Montmessin, F., Bertaux, J.L., 2010. NO emissions as observed by SPICAV during stellar occultations. Planet. Space Sci. 58, 1314–1326.

Sander et al., 2003. Chemical Kinetics and Photochemical Data for use in Atmospheric Studies. Evaluation Number 14. JPL Publication 02-25.

Schubert, G. et al., 2007. Venus Atmosphere: A Continuing Enigma, Exploring Venus as a Terrestrial Planet. American Geophysical Union, pp. 101–120.

Soret, L., Gérard, J.-C., Piccioni, G., Drossart, P., 2010. Venus OH nightglow distribution based on VIRTIS limb observations from Venus Express. Geophys. Res. Lett. 37, L06805. http://dx.doi.org/10.1029/2010GL042377.

Soret, L., Gérard, J.C., Montmessin, F., Piccioni, G., Drossart, P., Bertaux, J.L., 2012. Atomic oxygen on the Venus nightside: Global distribution deduced from airglow mapping. Icarus 217, 849–855.

Soret, L., Gérard, J.C., Piccioni, G., Drossart, P., 2014. Time variations of $O_2(a^1\Delta)$ nightglow spots on the Venus nightside and dynamics of the upper mesosphere. Icarus (in press). http://dx.doi.org/10.1016/j.icarus.2014.03.034.

Stewart, A.I.F., Gérard, J.C., Rusch, D.W., Bougher, S.W., 1980. Morphology of the Venus ultraviolet night airglow. J. Geophys. Res. 85, 7861–7870. http://dx.doi.org/10.1029/JA085iA13p07861.

Stiepen, A., Gérard, J.-C., Dumont, M., Cox, C., Bertaux, J.-L., 2013. Venus nitric oxide nightglow mapping from SPICAV nadir observations. Icarus 226, 428–436.

Svedhem, H. et al., 2007. Venus Express—The first European mission to Venus. Planet. Space Sci. 55, 1636–1652.

Taylor, F. et al., 1980. Structure and meteorology of the middle atmosphere of Venus: Infrared remote sensing from the Pioneer orbiter. J. Geophys. Res. 85, 7963–8006. http://dx.doi.org/10.1029/JA085iA13p07963.

Titov, D.V. et al., 2006. Venus Express science planning. Planet. Space Sci. 54, 1279–1297.

Von Zahn, U., Fricke, K.H., Hunten, D.M., Krankowsky, D., Mauersberger, K., Nier, A.O., 1980. The upper atmosphere of Venus during morning conditions. J. Geophys. Res. 85, 7829–7840. http://dx.doi.org/10.1029/JA085iA13p07829.

Zalucha, A.M., Brecht, A.S., Rafkin, S., Bougher, S.W.M., Alexander, J., 2013. Incorporation of a gravity wave momentum deposition parameterization into the Venus Thermosphere General Circulation Model (VTGCM). J. Geophys. Res. 118, 147–160. http://dx.doi.org/10.1029/2012JE004168.

Zhang, S., Bougher, S.W., Alexander, M.J., 1996. The impact of gravity waves on the Venus thermosphere and O_2 IR nightglow. J. Geophys. Res. 101, 23195–23205. http://dx.doi.org/10.1029/96JE02035.